Anisotropic superconductivity in the spin-vortex antiferromagnetic superconductor CaK(Fe$_{0.95}$Ni$_{0.05}$)$_4$As$_4$

José Benito Llorens,[1] Edwin Herrera [ORCID],[1] Víctor Barrena [ORCID],[1] Beilun Wu [ORCID],[1] Niclas Heinsdorf,[2] Vladislav Borisov,[2,3] Roser Valentí [ORCID],[2] William R. Meier [ORCID],[4] Sergey Bud'ko,[4] Paul C. Canfield,[4] Isabel Guillamón [ORCID],[1,*] and Hermann Suderow [ORCID][1]

[1]*Laboratorio de Bajas Temperaturas y Altos Campos Magnéticos, Departamento de Física de la Materia Condensada, Instituto Nicolás Cabrera and Condensed Matter Physics Center (IFIMAC), Unidad Asociada UAM-CSIC, Universidad Autónoma de Madrid, E-28049 Madrid, Spain*

[2]*Institut für Theoretische Physik, Goethe-Universität Frankfurt, Max-von-Laue-Strasse 1, 60438 Frankfurt am Main, Germany*

[3]*Department of Physics and Astronomy, Uppsala University, Box 516, SE-75120 Uppsala, Sweden*

[4]*Ames Laboratory, Ames and Department of Physics and Astronomy, Iowa State University, Ames, Iowa 50011, USA*

High critical temperature superconductivity often occurs in systems where an antiferromagnetic order is brought near $T = 0$ K by slightly modifying pressure or doping. CaKFe$_4$As$_4$ is a superconducting, stoichiometric iron-pnictide compound showing optimal superconducting critical temperature with T_c as large as 35 K. Doping with Ni induces a decrease in T_c and the onset of spin-vortex crystal (SVC) antiferromagnetic order, which consists of spins pointing inwards to or outwards from alternating As sites on the diagonals of the in-plane square Fe lattice. Here we study the band structure of CaK(Fe$_{0.95}$Ni$_{0.05}$)$_4$As$_4$ ($T_c = 10$ K, $T_{SVC} = 50$ K) using quasiparticle interference with a scanning tunneling microscope and show how the SVC modifies the band structure and induces a fourfold superconducting gap anisotropy.

Iron-pnictide superconductors mostly crystallize in a tetragonal structure. Optimal T_c appears in a phase diagram that shows structural, nematic, or magnetic order in the vicinity of superconductivity [1–5]. Whereas most Fe-based superconductors need doping (or pressure) to reach maximal T_c values, CaKFe$_4$As$_4$ is superconducting with the highest critical temperature in the pure stoichiometric compound with $T_c \approx 35$ K [6,7]. Elastoresistivity, nuclear magnetic resonance (NMR), and neutron-scattering experiments reveal magnetic fluctuations [8–10]. Contrary to other pnictide superconductors, there are neither structural modifications of the crystal when cooling nor strong electronic anisotropy in the form of nematicity [7,11]. The superconducting gap changes sign in different pockets of the Fermi surface and has $s\pm$ symmetry as many other iron pnictides [12–15]. Electron count and other physical properties such as T_c and pairing symmetry are similar to the nearly optimally doped (Ba$_{0.5}$K$_{0.5}$)Fe$_2$As$_2$ [12,16], where the magnetic order of BaFe$_2$As$_2$ is suppressed by hole doping with K.

Following this idea, electron doping CaKFe$_4$As$_4$ by substituting Co or Ni for Fe leads to antiferromagnetic order [Fig. 1(a)] [17]. However, the observed arrangement of magnetic moments is not the common, orthorhombic collinear antiferromagnetic (AFM) order that is characteristic of BaFe$_2$As$_2$ and many other iron-based superconductors, but instead is a different, noncollinear magnetic structure, called spin-vortex crystal (SVC). Furthermore, the onset of the SVC

phase is not accompanied by the emergence of any other order such as nematicity or a structural transition, making this system an ideal candidate to study the interplay between superconductivity and magnetism. The crystal structure is composed of Fe$_2$As$_2$ layers that are separated alternatingly with Ca and K [6]. These alternating layers reduce crystal symmetry and lead to the noncollinear SVC [17,18]. SVC consists of a radial pattern of Fe moments around the blue As1 sites depicted in the inset of Fig. 1(b). SVC magnetism is closely related to the other magnetic orders observed in the Fe-based superconductors, but retains tetragonal symmetry [19–22]. There is robust experimental evidence for the presence of the SVC within the superconducting phase [17,23–26]. The situation offered by doped CaKFe$_4$As$_4$ raises a question relevant to iron-pnictide superconductivity. What is the effect, if any, of the arrangement of magnetic moments on the superconducting gap anisotropy? Here we study the local density of states of CaK(Fe$_{0.95}$Ni$_{0.05}$)$_4$As$_4$ ($T_{SVC} = 50$ K and $T_c = 10$ K) via scanning tunneling microscopy (STM). We determine the band structure in the magnetic phase and show that the superconducting gap size is connected to the arrangement of magnetic moments inside the unit cell, being smaller along directions where there is a nonzero magnetic moment.

We study single crystals of CaK(Fe$_{0.95}$Ni$_{0.05}$)$_4$As$_4$, which have been obtained using the method of Refs. [11,17]. Crystals were screened to present the same resistivity vs. temperature as shown in [17]. Samples were mounted into a dilution refrigerator STM as described in Ref. [27]. We provide further details of the crystals, low-temperature cleaving mechanism, and data analysis in the Supplemental Material [28] (see, also, Refs. [27,29–38] therein).
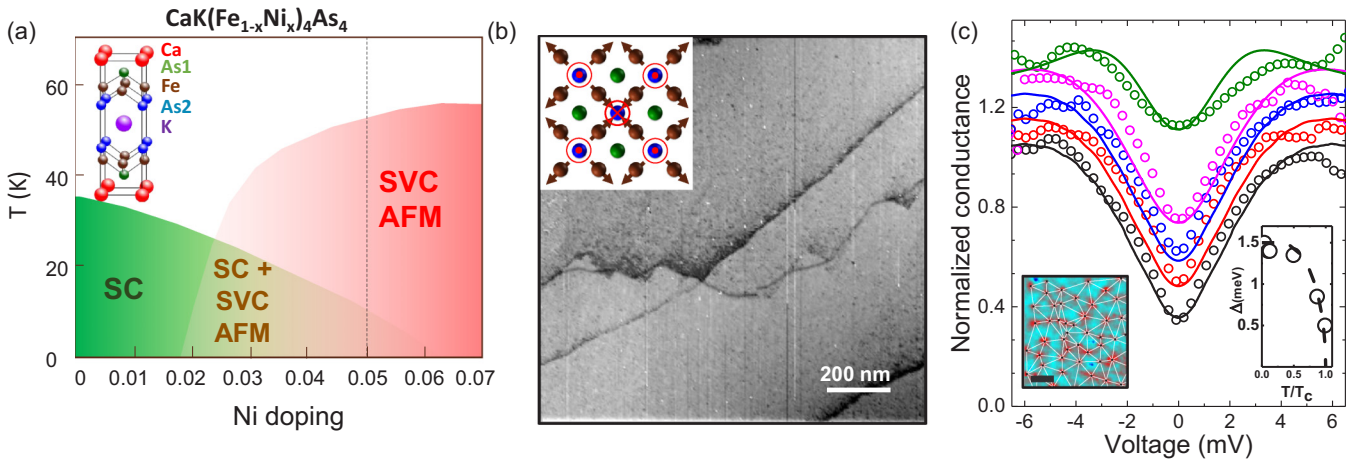
*isabel.guillamon@uam.es

FIG. 1. (a) Schematic phase diagram of Ni-doped $CaKFe_4As_4$, with a dashed vertical line indicating the Ni concentration discussed here. Crystalline structure of $CaK(Fe_{0.95}Ni_{0.05})_4As_4$ is shown in the upper left inset. (b) STM topographic image of the surface of $CaK(Fe_{0.95}Ni_{0.05})_4As_4$. The difference between black and white corresponds to a height change of 0.3 nm. In the inset, we show a view from the top of the structure, indicating Fe (brown) and As (As1 in blue and As2 in green) atoms and with arrows indicating the magnetic moments in the SVC. Note that the magnetic moments point towards As1, giving a finite hyperfine field pointing upwards along the c axis (red circles with a cross), and from As1 atoms, giving a hyperfine field pointing downwards along the c axis (red circle with a dot) [17]. At As2, the field cancels. (c) The temperature dependence of the tunneling conductance is shown as open circles in the main panel (the conductance is normalized to its value at voltages well above the superconducting gap). Curves are taken (from bottom to top) at 0.3, 0.8, 1.4, 4,0, and 7.0 K in the same field of view as in (b) (and in Fig. 1 of the Supplemental Material [28]). Lines are fits using the density of states obtained for a distribution of values of the superconducting gap. Curves are shifted vertically for clarity. The bottom right inset shows as black open circles the temperature dependence of the superconducting gap value, extracted from the maximum in the derivative of the density of states as a function of temperature normalized to T_c. The dashed line is a guide to the eye. Bottom left inset provides an image of the vortex lattice taken at 0.3 K and 2.0 T. Color scale shows the normalized zero-bias conductance, which goes from the normal state value (1.0, red) to its value at zero field (0.4, blue). White lines are the Delaunay triangulation of vortex positions, which are shown as black dots. Black scale bar is 30 nm long. Further vortex lattice images and details are provided in the Supplemental Material [28] (see, also, Refs. [13,39,40] therein).

Figure 1(b) shows a typical surface obtained for $CaK(Fe_{0.95}Ni_{0.05})_4As_4$, which resembles surfaces obtained in pure $CaKFe_4As_4$ [13]. We identify atomically flat areas over a scanning window several μm in size, separated by atomic-size trenches [black lines in Fig. 1(b)]. Figure 1(c) displays the tunneling conductance $G = dI/dV$ in the same field of view. The superconducting gap manifests as the usual, strong reduction of the tunneling conductance for voltages of the order of a few mV, which disappears at about T_c. The zero-bias density of states is large and finite and the coherence peaks are strongly smeared. The shape of the superconducting tunneling conductance remains the same over large areas. Vortex lattice images under magnetic fields clearly present a disordered hexagonal vortex lattice (lower left inset of Fig. 1(c) and Supplemental Material [28]) with a homogeneous background of tunneling conductance curves similar to those shown in Fig. 1(c). To estimate the superconducting gap at zero field in $CaK(Fe_{0.95}Ni_{0.05})_4As_4$, we construct a superconducting density of states $N(E)$ allowing for a large distribution of values of the superconducting gap and including a finite density of states at the Fermi level (see details in the Supplemental Material [28]; see, also, Refs. [32,41] therein), which gives the tunneling conductance as solid lines in the main panel of Fig. 1(c). The lower right inset of Fig. 1(c) shows the energy at which the derivative of $N(E)$, $\frac{dN}{dE}$, has a maximum. We obtain 1.5 meV at low temperatures, which is very similar to the gap value estimated from $T_c \approx 10$ K, $\Delta \approx 1.5$ meV. This value decreases with temperature, as shown in the lower right panel

of Fig. 1(c). These results are completely different from those observed in pure $CaKFe_4As_4$, where a two-gap structure with a few states at the Fermi level is found [12,13].

When zooming into a small region, we observe electronic scattering due to defects. The field of view shown in the topographic constant current image of Fig. 2(a) is atomically flat. There are atomic-size defects (black spots) and there is a wavy background. We can then build tunneling conductance maps as a function of the bias voltage V using $G(V)$ at each point (x, y) of the field of view. A representative example is shown in Figs. 2(b)–2(f) for a few bias voltages V. $G(V)$ is quite homogeneous and does not change much close to atomic-size defects, but we can clearly identify a wavy background whose wavelength changes with V. The contribution of scattered electrons to $G(V)$ leads to a quasiparticle interference pattern and is proportional to the densities of states of the initial and final states, i.e., the joint density of states. The quasiparticle scattering wavelength is equal to the difference q between the initial and final scattering wave vectors [13,42]. The Fourier transform of the tunneling conductance images is shown in Figs. 2(g)–2(k). We identify three main scattering vectors: q_α, q_β, and q_γ. The largest scattering vector, q_γ, is slightly anisotropic, being larger along the $\overline{\Gamma}\text{-}\overline{X}$ direction than along $\overline{\Gamma}\text{-}\overline{M}$ (the notation of the Brillouin-zone directions follows the one proposed for pnictide superconductors in Ref. [43]). The Fourier amplitude at the three scattering vectors decreases close to the Fermi level due to the opening of the superconducting gap [Fig. 2(i)].
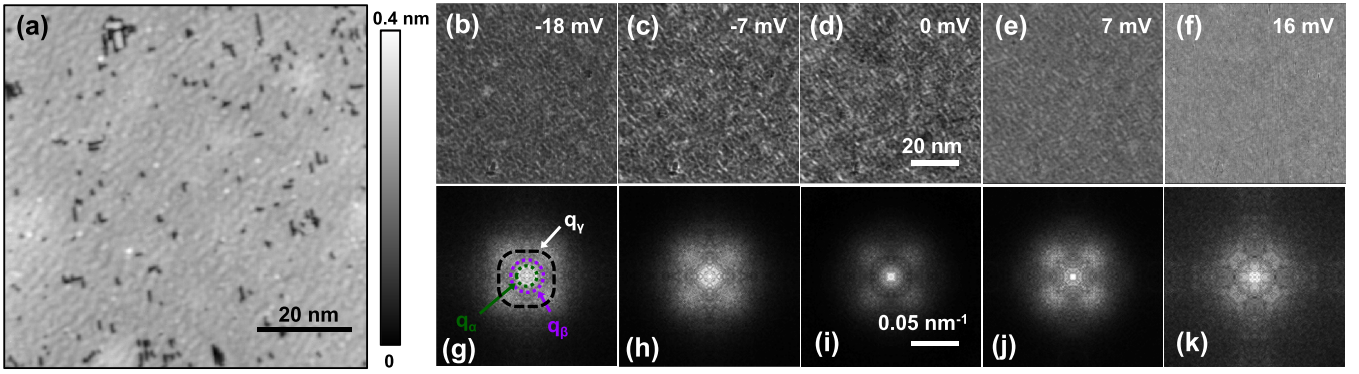
FIG. 2. (a) Topography of the area where we have made the quasiparticle interference experiment shown in (b)–(k). The colorscale bar is given in the bottom right and the gray scale by the bar at the right. The image has been taken at a bias voltage of 30 mV and a current of 1.0 nA at zero magnetic field and at 0.3 K. (b)–(f) Tunneling conductance normalized to voltages above 40 mV as a function of the position for a few representative bias voltages (given in each panel). The lateral scale bar is provided in (d). The gray scale corresponds to modulations of about 15% of the normalized conductance at each bias voltage. (g)–(k) Fourier transform, symmetrized taking into account the in-plane square lattice, of (b)–(f) shown in the first Brillouin zone. In (g), we mark the outer main scattering vector (black dashed circle) as well as the two inner scattering vectors (purple and green dashed circles). The lateral scale bar is given in (i) and the gray scale goes from low (black) to large (white) scattering intensity.

When plotting the bias voltage dependence of the scattering pattern along the high-symmetry directions $\overline{\Gamma}$-$\overline{X}$ and $\overline{\Gamma}$-$\overline{M}$ [Figs. 3(a) and 3(b), respectively], we observe that all scattering vectors q decrease in size when increasing the bias voltage above the Fermi level. The qualitative behavior is very similar for both high-symmetry directions, although the values of q_γ are slightly larger for $\overline{\Gamma}$-$\overline{X}$ than for $\overline{\Gamma}$-$\overline{M}$. The reduction of the intensity inside the superconducting gap is band dependent. The superconducting gap is most clearly observed for the largest scattering vector q_γ.

In Fig. 3(c), we show the scattering intensity around zero bias and at q_γ as a function of the angle, with $\theta = 0°$ for $\overline{\Gamma}$-$\overline{X}$ and $\theta = 45°$ for $\overline{\Gamma}$-$\overline{M}$. We find a fourfold modulation of the superconducting density of states which is not present in the stoichiometric compound and follows the symmetry of the SVC [12,13] (see, also, Fig. 3 in the Supplemental Material [28] for results in the pure compound). The superconducting gap is larger along the direction where the hyperfine field on the As1 sites cancels [$\overline{\Gamma}$-$\overline{X}$; orange lines in Fig. 3(c)], whereas it is smaller when the hyperfine field remains finite [$\overline{\Gamma}$-$\overline{M}$, green lines in Fig. 3(c)], suggesting a competition between superconductivity and magnetism. We will analyze this observation further below.

In what follows, we investigate the origin of the three scattering vectors identified in Figs. 3(a) and 3(b). We have calculated the electronic structure of CaKFe$_4$As$_4$ and CaK(Fe$_{0.95}$Ni$_{0.05}$)$_4$As$_4$ in the tetragonal paramagnetic phase within density functional theory as described in Ref. [28] (see, also, Refs. [44–56] therein). The effect of Ni doping has been taken into account with the virtual crystal approximation (VCA). In Figs. 4(a) and 4(b), we show the respective Fermi surfaces. As expected, upon Ni doping, the inner hole pockets slightly shrink in CaK(Fe$_{0.95}$Ni$_{0.05}$)$_4$As$_4$ [Fig. 4(b)] as compared to the pure compound [Fig. 4(a)] with the overall structure of the Fermi surface remaining similar. Our measurements [e.g., Figs. 3(a) and 3(b)] show, however, that the scattering pattern is very different. In CaKFe$_4$As$_4$ [13], the scattering pattern consists of a single scattering vector,

associated to interband scattering between two hole bands centered at the Brillouin zone that increases strongly in size when increasing the bias voltage. In CaK(Fe$_{0.95}$Ni$_{0.05}$)$_4$As$_4$, there are three vectors whose size decreases much less drastically above the Fermi level. The SVC magnetic order invokes a folding of the band structure along the AFM wave vector due to the doubling of the unit cell [see inset in Fig. 4(c)]. We assume that folding is the main consequence of the SVC in the band structure. The folded electron bands are shown in Fig. 4(c) and the Fermi surface in Fig. 4(d). The bands at the edges of the unfolded Brillouin zone are now centered around $\overline{\Gamma}$, providing a clearly defined set of bands coexisting in the same Brillouin-zone region as the hole pockets centered at $\overline{\Gamma}$. In the calculated bands, we identify three scattering vectors between hole and electron bands whose size corresponds to the observed q_α, q_β, and q_γ vectors [arrows in Figs. 4(c) and 4(d)]. Their value decreases with increasing bias voltage, as is also found experimentally [Figs. 3(a) and 3(b)]. Thus, the reconstructed Fermi surface provides an accurate description of the band structure of CaK(Fe$_{0.95}$Ni$_{0.05}$)$_4$As$_4$.

We now discuss the observed fourfold modulation of the superconducting gap in CaK(Fe$_{0.95}$Ni$_{0.05}$)$_4$As$_4$ [Fig. 3(c)], which is not present in the stoichiometric compound [12,13]. It is quite remarkable that the minimum gap value occurs along the direction where the c-axis oriented magnetic field adds up in the unit cell [green lines in Fig. 3(c), right panel].

A fourfold modulated superconducting gap has been found previously in different nonmagnetic pnictide superconductors and can often be related to band structure anisotropy [57–61]. An anisotropic gap was found on electron pockets of the system NaFe$_{1-x}$Co$_x$As, where a spin density wave coexists with superconductivity [62,63]. This material, as well as other iron-pnictide superconductors, has strong nematic fluctuations which share symmetry properties of the antiferromagnetic order, making it difficult to disentangle the influence of both effects on superconductivity. No nematicity has been reported yet for the CaKFe$_4$As$_4$ family. There is an anticorrelation between the superconducting and spin density wave gap in
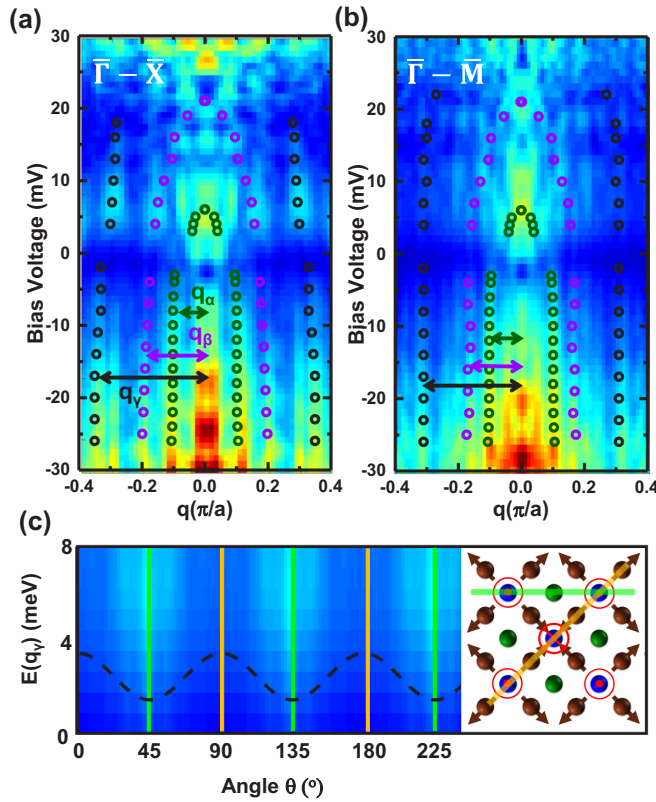
FIG. 3. Scattering intensity for the two main symmetry directions, (a) $\overline{\Gamma}$-$\overline{X}$ and (b) $\overline{\Gamma}$-$\overline{M}$. Open circles mark the evolution of the scattering vectors with bias voltage. Scattering vectors q_α, q_β, and q_γ are shown in green, violet, and black. Color scale goes from low (blue) to high (red) scattering intensity. (c) Scattering intensity as a function of the angle with respect to the in-plane *a* axis for energies close to the Fermi level in q_γ. Color scale goes from blue (about 0.4 in normalized conductance units) to cyan (about 1.0 in normalized conductance units). The black dashed line schematically shows a modulation of the scattering intensity at q_γ (the modulation represented in the figure is by about 50% of the normalized tunneling conductance, taken at a bias voltages of approximately half the gap). The vertical light-green and orange lines highlight the $\overline{\Gamma}$-$\overline{M}$ and $\overline{\Gamma}$-$\overline{X}$ directions, respectively. The right panel shows a schematic representation of the lattice, with Fe atoms in brown (and their spins represented by arrows), As1 in blue, and As2 in green, and the symmetry directions used in previous figures as light-green and orange lines. The hyperfine field is shown by red circles with a dot and red circles with a cross. Notice that the hyperfine field adds to zero along the orange lines and is finite along the green lines.

NaFe$_{1-x}$Co$_x$As, although the spin density wave itself has a zero-average magnetic moment along all crystalline directions and both phenomena occur in different parts of the Fermi surface [63–65]. The behavior we find here has not been observed in the iron-pnictide superconducting family, as it directly connects the anisotropic structure of the local magnetic order with the anisotropic superconducting gap.

Finally, we discuss the observation of a large zero-bias tunneling conductance at the Fermi level, which contrasts the zero value found in pure CaKFe$_4$As$_4$ [12,13]. There is no visible difference on the surface termination between Ni-doped and pristine CaKFe$_4$As$_4$. Pure CaKFe$_4$As$_4$ presents,

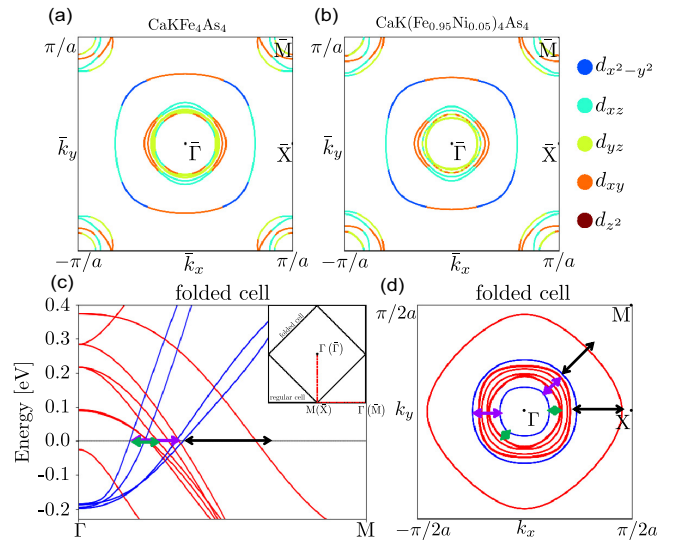FIG. 4. Fermi surface of (a) pure CaKFe$_4$As$_4$ and (b) CaK(Fe$_{0.95}$Ni$_{0.05}$)$_4$As$_4$ in the paramagnetic phase, obtained as described in the text. (c),(d) Band structure and Fermi surface of CaK(Fe$_{0.95}$Ni$_{0.05}$)$_4$As$_4$ in the folded AFM Brillouin zone. Folded bands are shown in blue. Black, violet, and green arrows are the main scattering vectors shown in Fig. 3. The convention for the names of the directions of folded and unfolded Brillouin zones [inset of (c)] follows Ref. [43].

at some locations, a finite zero-bias conductance due to pair breaking associated with scattering between portions of the Fermi surface with a different gap sign [13]. London penetration depth measurements in electron irradiated crystals of CaK(Fe$_{0.95}$Ni$_{0.05}$)$_4$As$_4$ suggest an anisotropic superconducting gap with $s\pm$ symmetry, with the anisotropy decreasing with disorder [66]. The increased gap anisotropy that we observe is unlikely due to disorder-induced pair breaking [67]. While the latter may certainly play a role, the role of magnetism seems relevant too. NMR experiments, Mössbauer spectroscopy, and muon spin rotation/relaxation studies have shown evidence for the coexistence between superconductivity and magnetic order in CaK(Fe$_{0.95}$Ni$_{0.05}$)$_4$As$_4$ [23–25]. The ordered magnetic moment is gradually suppressed when entering in the superconducting phase, suggesting that superconductivity and magnetism are competing for the same electrons [24,24–26,68]. Furthermore, the absence of glide symmetry may lead to a spin-current density wave, or *d*-density wave [69]. The chiral properties of a spin-current density wave lead to a pattern of currents inside the unit cell [69–72]. Thus, the finite density of states at low energies is a consequence of competing interactions between magnetism and superconductivity and the influence of SVC on the superconducting properties.

In conclusion, we have measured the spatial dependence of the tunneling conductance in the SVC state of CaK(Fe$_{0.95}$Ni$_{0.05}$)$_4$As$_4$ and report direct evidence for a strong mutual influence between superconductivity and SVC antiferromagnetic order. Quasiparticle interference measurements supported by band structure calculations demonstrate a Fermi-surface reconstruction and anisotropic pairing through an in-plane fourfold modulation of the superconducting gap.

The comparison to $CaKFe_4As_4$, where there is no antiferromagnetic order and the superconducting gap shows no in-plane anisotropy, strongly suggests that the SVC antiferromagnetic state is responsible for the anisotropic pairing in $CaK(Fe_{0.95}Ni_{0.05})_4As_4$.

[1] Y. Kamihara, T. Watanabe, M. Hirano, and H. Hosono, Iron-based layered superconductor La[$O_{1-x}F_x$]FeAs ($x = 0.050.12$) with $T_c = 26$ K, J. Am. Chem. Soc. **130**, 3296 (2008).

[2] P. C. Canfield and S. L. Bud'ko, FeAs-based superconductivity: A case study of the effects of transition metal doping on $BaFe_2As_2$, Annu. Rev. Condens. Matter Phys. **1**, 27 (2010).

[3] J. Paglione and R. L. Greene, High-temperature superconductivity in iron-based materials, Nat. Phys. **6**, 645 (2010).

[4] P. J. Hirschfeld, M. M. Korshunov, and I. I. Mazin, Gap symmetry and structure of Fe-based superconductors, Rep. Prog. Phys. **74**, 124508 (2011).

[5] H. Hosono and K. Kuroki, Iron-based superconductors: Current status of materials and pairing mechanism, Physica C: Superconduct. Applic. **514**, 399 (2015).

[6] A. Iyo, K. Kawashima, T. Kinjo, T. Nishio, S. Ishida, H. Fujihisa, Y. Gotoh, K. Kihou, H. Eisaki, and Y. Yoshida, New-structure-type Fe-based superconductors: $CaAFe_4As_4$ (A = K, Rb, Cs) and $SrAFe_4As_4$ (A = Rb, Cs), J. Am. Chem. Soc. **138**, 3410 (2016).

[7] W. R. Meier, T. Kong, U. S. Kaluarachchi, V. Taufour, N. H. Jo, G. Drachuck, A. E. Böhmer, S. M. Saunders, A. Sapkota, A. Kreyssig, M. A. Tanatar, R. Prozorov, A. I. Goldman, F. F. Balakirev, A. Gurevich, S. L. Bud'ko, and P. C. Canfield, Anisotropic thermodynamic and transport properties of single-crystalline $CaKFe_4As_4$, Phys. Rev. B **94**, 064501 (2016).

[8] W.-L. Zhang, W. R. Meier, T. Kong, P. C. Canfield, and G. Blumberg, High-T_c superconductivity in $CaKFe_4As_4$ in absence of nematic fluctuations, Phys. Rev. B **98**, 140501(R) (2018).

[9] J. Cui, Q.-P. Ding, W. R. Meier, A. E. Böhmer, T. Kong, V. Borisov, Y. Lee, S. L. Bud'ko, R. Valentí, P. C. Canfield, and Y. Furukawa, Magnetic fluctuations and superconducting properties of $CaKFe_4As_4$ studied by ^{75}As NMR, Phys. Rev. B **96**, 104512 (2017).

[10] K. Iida, M. Ishikado, Y. Nagai, H. Yoshida, A. D. Christianson, N. Murai, K. Kawashima, Y. Yoshida, H. Eisaki, and A. Iyo, Spin resonance in the new-structure-type iron-based superconductor $CaKFe_4As_4$, J. Phys. Soc. Jpn. **86**, 093703 (2017).

[11] W. R. Meier, T. Kong, S. L. Bud'ko, and P. C. Canfield, Optimization of the crystal growth of the superconductor $CaKFe_4As_4$ from solution in the $FeAs$-$CaFe_2As_2$-KFe_2As_2 system, Phys. Rev. Materials **1**, 013401 (2017).

[12] K. Cho, A. Fente, S. Teknowijoyo, M. A. Tanatar, K. R. Joshi, N. M. Nusran, T. Kong, W. R. Meier, U. Kaluarachchi, I. Guillamón, H. Suderow, S. L. Bud'ko, P. C. Canfield, and R. Prozorov, Nodeless multiband superconductivity in stoichiometric single-crystalline $CaKFe_4As_4$, Phys. Rev. B **95**, 100502(R) (2017).

[13] A. Fente, W. R. Meier, T. Kong, V. G. Kogan, S. L. Bud'ko, P. C. Canfield, I. Guillamón, and H. Suderow, Influence of multiband sign-changing superconductivity on vortex cores and vortex pinning in stoichiometric high-T_c $CaKFe_4As_4$, Phys. Rev. B **97**, 134501 (2018).

[14] D. Mou, T. Kong, W. R. Meier, F. Lochner, Lin-Lin Wang, Q. Lin, Y. Wu, S. L. Bud'ko, I. Eremin, D. D. Johnson, P. C. Canfield, and A. Kaminski, Enhancement of the Superconducting Gap by Nesting in $CaKFe_4As_4$: A New High Temperature Superconductor, Phys. Rev. Lett. **117**, 277001 (2016).

[15] G. A. Ummarino, Phenomenology of $CaKFe_4As_4$ explained in the framework of four bands Eliashberg theory, Physica C: Superconduct. Applic. **529**, 50 (2016).

[16] D. Jost, J.-R. Scholz, U. Zweck, W. R. Meier, A. E. Böhmer, P. C. Canfield, N. Lazarević, and R. Hackl, Indication of subdominant d-wave interaction in superconducting $CaKFe_4As_4$, Phys. Rev. B **98**, 020504(R) (2018).

[17] W. R. Meier, Qing-Ping Ding, A. Kreyssig, S. L. Bud'ko, A. Sapkota, K. Kothapalli, V. Borisov, R. Valentí, C. D. Batista, P. P. Orth, R. M. Fernandes, A. I. Goldman, Y. Furukawa, A. E. Böhmer, and P. C. Canfield, Hedgehog spin-vortex crystal stabilized in a hole-doped iron-based superconductor, npj Quantum Mater. **3**, 5 (2018).

[18] W. Meier, Growth, properties and magnetism of $CaKFe_4As_4$, Ph.D. thesis, Iowa State University, 2018.

[19] X. Wang, J. Kang, and R. M. Fernandes, Magnetic order without tetragonal-symmetry-breaking in iron arsenides: Microscopic mechanism and spin-wave spectrum, Phys. Rev. B **91**, 024401 (2015).

[20] M. H. Christensen, J. Kang, B. M. Andersen, I. Eremin, and R. M. Fernandes, Spin reorientation driven by the interplay between spin-orbit coupling and Hund's rule coupling in iron pnictides, Phys. Rev. B **92**, 214509 (2015).

[21] M. Hoyer, R. M. Fernandes, A. Levchenko, and J. Schmalian, Disorder-promoted C_4-symmetric magnetic order in iron-based superconductors, Phys. Rev. B **93**, 144414 (2016).

[22] Q-P. Ding, W. R. Meier, J. Cui, M. Xu, A. E. Böhmer, S. L. Bud'ko, P. C. Canfield, and Y. Furukawa, Hedgehog Spin-Vortex Crystal Antiferromagnetic Quantum Criticality in CaK(Fe$_{1-x}$Ni$_x$)$_4$ as Revealed by NMR, Phys. Rev. Lett. **121**, 137204 (2018).

[23] Q-P. Ding, W. R. Meier, A. E. Böhmer, S. L. Bud'ko, P. C. Canfield, and Y. Furukawa, NMR study of the new magnetic superconductor CaK(Fe$_{0.951}$Ni$_{0.049}$)$_4$As$_4$: Microscopic coexistence of the hedgehog spin-vortex crystal and superconductivity, Phys. Rev. B **96**, 220510(R) (2017).

[24] S. L. Bud'ko, V. G. Kogan, R. Prozorov, W. R. Meier, M. Xu, and P. C. Canfield, Coexistence of superconductivity and magnetism in CaK(Fe$_{1-x}$Ni$_x$)$_4$As$_4$ as probed by ^{57}Fe Mössbauer spectroscopy, Phys. Rev. B **98**, 144520 (2018).

[25] R. Khasanov, G. Simutis, Y. G. Pashkevich, T. Shevtsova, W. R. Meier M. Xu, S. L. Bud'ko, V. G. Kogan, and P. C. Canfield, Magnetism and its coexistence with superconductivity in CaK(Fe$_{0.949}$Ni$_{0.051}$)$_4$As$_4$: Muon spin rotation/relaxation studies, Phys. Rev. B **102**, 094504 (2020).

[26] A. Kreyssig, J. M. Wilde, A. E. Böhmer, W. Tian, W. R. Meier, B. Li, B. G. Ueland, M. Xu, S. L. Bud'ko, P. C. Canfield *et al.*, Antiferromagnetic order in CaK(Fe$_{1-x}$Ni$_x$)$_4$As$_4$ and its interplay with superconductivity, Phys. Rev. B **97**, 224521 (2018).

[27] H. Suderow, I. Guillamon, and S. Vieira, Compact very low temperature scanning tunneling microscope with mechanically driven horizontal linear positioning stage, Rev. Sci. Instrum. **82**, 033711 (2011).

[28] See Supplemental Material at http://link.aps.org/supplemental/10.1103/PhysRevB.103.L060506 for further details on the experimental setup, atomic resolution images, results on the undoped compound, on the superconducting vortex lattice, and further details on the density functional calculations.

[29] I. Guillamón, R. Córdoba, J. Sesé, J. De Teresa, M. R. Ibarra, S. Vieira, and H. Suderow, Enhancement of long-range correlations in a 2D vortex lattice by an incommensurate 1D disorder potential, Nat. Phys. **10**, 851 (2014).

[30] A. Fente, A. Correa-Orellana, A. E. Böhmer, A. Kreyssig, S. Ran, S. L. Bud'ko, P. C. Canfield, F. J. Mompean, M. García-Hernández, C. Munuera, I. Guillamón, and H. Suderow, Direct visualization of phase separation between superconducting and nematic domains in Co-doped CaFe$_2$As$_2$ close to a first-order phase transition, Phys. Rev. B **97**, 014505 (2018).

[31] I. Guillamón, H. Suderow, S. Vieira, L. Cario, P. Diener, and P. Rodière, Superconducting Density of States and Vortex Cores of 2H-NbS$_2$, Phys. Rev. Lett. **101**, 166407 (2008).

[32] M. Crespo, H. Suderow, S. Vieira, S. Bud'ko, and P. C. Canfield, Local Superconducting Density of States of ErNi$_2$B$_2$C, Phys. Rev. Lett. **96**, 027003 (2006).

[33] M. Bristow, W. Knafo, P. Reiss, W. Meier, P. C. Canfield, S. J. Blundell, and A. I. Coldea, Competing pairing interactions responsible for the large upper critical field in a stoichiometric iron-based superconductor CaKFe$_4$As$_4$, Phys. Rev. B **101**, 134502 (2020).

[34] J. A. Galvis, E. Herrera, I. Guillamón, J. Azpeitia, R. F. Luccas, C. Munuera, M. Cuenca, J. A. Higuera, N. Díaz, M. Pazos, M. García-Hernandez, A. Buendía, S. Vieira, and H. Suderow, Three axis vector magnet set-up for cryogenic scanning probe microscopy, Rev. Sci. Instrum. **86**, 013706 (2015).

[35] R. Á. Montoya, S. Delgado, J. Castilla, J. Navarrete, N. D. Contreras, J. R. Marijuan, V. Barrena, I. Guillamón, and

[36] I. Guillamon, H. Suderow, S. Vieira, and P. Rodiere, Scanning tunneling spectroscopy with superconducting tips of Al, Physica C: Superconduct. Applic. **468**, 537 (2008).

[37] F. Martin, V. Barrena, J. Benito, I. Guillamon, and H. Suderow, Cryogenic microscope operation and image treatment (2021), doi:10.5281/zenodo.4546199, doi:10.5281/zenodo.4546203.

[38] I. Horcas, R. Fernández, J. M. Gómez-Rodríguez, J. Colchero, J. Gómez-Herrero, and A. M. Baro, Wsxm: A software for scanning probe microscopy and a tool for nanotechnology, Rev. Sci. Instrum. **78**, 013705 (2007).

[39] N. Haberkorn, M. Xu, W. R. Meier, J. Schmidt, S. L. Bud'ko, and P. C. Canfield, Effect of Ni doping on vortex pinning in CaK(Fe$_{1-x}$Ni$_x$)$_4$As$_4$ single crystals, Phys. Rev. B **100**, 064524 (2019).

[40] W. Liu, L. Cao, S. Zhu, L. Kong, G. Wang, M. Papaj, P. Zhang, Ya-Bin Liu, H. Chen, G. Li, F. Yang, T. Kondo, S. Du, Guang-Han Cao, S. Shin, L. Fu, Z. Yin, Hong-Jun Gao, and H. Ding, A new Majorana platform in an Fe-As bilayer superconductor, Nat. Commun. **11**, 5688 (2020).

[41] V. S. Stolyarov, K. S. Pervakov, A. S. Astrakhantseva, I. A. Golovchanskiy, D. V. Vyalikh, T. K. Kim, S. V. Eremeev, V. A. Vlasenko, V. M. Pudalov, A. A. Golubov, E. V. Chulkov, and D. Roditchev, Electronic structures and surface reconstructions in magnetic superconductor RbEuFe$_4$As$_4$, J. Phys. Chem. Lett. **11**, 9393 (2020).

[42] J. E. Hoffman, Spectroscopic scanning tunneling microscopy insights into Fe-based superconductors, Rep. Prog. Phys. **74**, 124513 (2011).

[43] O.K. Andersen and L. Boeri, On the multi-orbital band structure and itinerant magnetism of iron-based superconductors, Ann. Phys. **523**, 8 (2011).

[44] J. P. Perdew and Y. Wang, Accurate and simple analytic representation of the electron-gas correlation energy, Phys. Rev. B **45**, 13244 (1992).

[45] J. P. Perdew, K. Burke, and M. Ernzerhof, Generalized Gradient Approximation Made Simple, Phys. Rev. Lett. **77**, 3865 (1996).

[46] K. Koepernik and H. Eschrig, Full-potential nonorthogonal local-orbital minimum-basis band-structure scheme, Phys. Rev. B **59**, 1743 (1999).

[47] I. Opahle, K. Koepernik, and H. Eschrig, Full-potential band-structure calculation of iron pyrite, Phys. Rev. B **60**, 14035 (1999).

[48] H. Eschrig, M. Richter, and I. Opahle, Relativistic solid state calculations, in *Relativistic Electronic Structure Theory*, Theoretical and Computational Chemistry Vol. 14, edited by Peter Schwerdtfeger (Elsevier, Amsterdam, 2004), pp. 723–776.

[49] H. Eschrig, K. Koepernik, and I. Chaplygin, Density functional application to strongly correlated electron systems, J. Solid State Chem. **176**, 482 (2003).

[50] H. Eschrig, *The Fundamentals of Density Functional Theory*, Vol. 176 (B. G. Teubner Verlagsgesellschaft, Stuttgart, Leipzig, 1996).

[51] K. Lejaeghere *et al.*, Reproducibility in density functional theory calculations of solids, Science **351**, aad3000 (2016).

[52] L. Bellaiche and D. Vanderbilt, Virtual crystal approximation revisited: Application to dielectric and piezoelectric properties of perovskites, Phys. Rev. B **61**, 7877 (2000).

H. Suderow, Methods to simplify cooling of liquid helium cryostats, HardwareX **5**, e00058 (2019).

[53] G. Kresse and J. Hafner, *Ab initio* molecular dynamics for liquid metals, Phys. Rev. B **47**, 558 (1993).

[54] G. Kresse and J. Furthmüller, Efficiency of *ab initio* total energy calculations for metals and semiconductors using a plane-wave basis set, Comput. Mater. Sci. **6**, 15 (1996).

[55] G. Kresse and J. Furthmüller, Efficient iterative schemes for *ab initio* total-energy calculations using a plane-wave basis set, Phys. Rev. B **54**, 11169 (1996).

[56] L. Nordheim, On the electron theory of metals. I, Ann. Phys. **401**, 607 (1931).

[57] K. Umezawa, Y. Li, H. Miao, K. Nakayama, Z.-H. Liu, P. Richard, T. Sato, J. B. He, D.-M. Wang, G. F. Chen, H. Ding, T. Takahashi, and S.-C. Wang, Unconventional Anisotropic *s*-Wave Superconducting Gaps of the LiFeAs Iron-Pnictide Superconductor, Phys. Rev. Lett. **108**, 037002 (2012).

[58] K. Okazaki, Y. Ito, Y. Ota, Y. Kotani, T. Shimojima, T. Kiss, S. Watanabe, C. T. Chen, S. Niitaka, T. Hanaguri, H. Takagi, A. Chainani, and S. Shin, Evidence for a $\cos(4\varphi)$ Modulation of the Superconducting Energy Gap of Optimally Doped FeTe$_{0.6}$Se$_{0.4}$ Single Crystals Using Laser Angle-Resolved Photoemission Spectroscopy, Phys. Rev. Lett. **109**, 237011 (2012).

[59] K. Okazaki, Y. Ota, Y. Kotani, W. Malaeb, Y. Ishida, T. Shimojima, T. Kiss, S. Watanabe, C.-T. Chen, K. Kihou, C. H. Lee, A. Iyo, H. Eisaki, T. Saito, H. Fukazawa, Y. Kohori, K. Hashimoto, T. Shibauchi, Y. Matsuda, H. Ikeda, H. Miyahara, R. Arita, A. Chainani, and S. Shin, Octet-line node structure of superconducting order parameter in KFe$_2$As$_2$, Science **337**, 1314 (2012).

[60] D. V. Evtushinsky, D. S. Inosov, V. B. Zabolotnyy, A. Koitzsch, M. Knupfer, B. Büchner, M. S. Viazovska, G. L. Sun, V. Hinkov, A. V. Boris, C. T. Lin, B. Keimer, A. Varykhalov, A. A. Kordyuk, and S. V. Borisenko, Momentum dependence of the superconducting gap in Ba$_{1-x}$K$_x$Fe$_2$As$_2$, Phys. Rev. B **79**, 054517 (2009).

[61] Y. Zhang, Z. R. Ye, Q. Q. Ge, F. Chen, J. Jiang, M. Xu, B. P. Xie, and D. L. Feng, Nodal superconducting-gap structure in ferropnictide superconductor BaFe$_2$(As$_{0.7}$P$_{0.3}$)$_2$, Nat. Phys. **8**, 371 (2012).

[62] Q. Q. Ge, Z. R. Ye, M. Xu, Y. Zhang, J. Jiang, B. P. Xie, Y. Song, C. L. Zhang, P. Dai, and D. L. Feng, Anisotropic But Nodeless Superconducting Gap in the Presence of Spin-Density Wave in Iron-Pnictide Superconductor NaFe$_{1-x}$Co$_x$As, Phys. Rev. X **3**, 011020 (2013).

[63] P. Cai, X. Zhou, W. Ruan, A. Wang, X. Chen, Dung-Hai Lee, and Y. Wang, Visualizing the microscopic coexistence of spin density wave and superconductivity in underdoped NaFe$_{1x}$Co$_x$As, Nat. Commun. **4**, 1596 (2013).

[64] P. Dai, Antiferromagnetic order and spin dynamics in iron-based superconductors, Rev. Mod. Phys. **87**, 855 (2015).

[65] M. M. Korshunov, Effect of gap anisotropy on the spin resonance peak in the superconducting state of iron-based materials, Phys. Rev. B **98**, 104510 (2018).

[66] S. Teknowijoyo, K. Cho, M Kończykowski, E. I. Timmons, M. A. Tanatar, W. R. Meier, M. Xu, S. L. Bud'ko, P. C. Canfield, and R. Prozorov, Robust $s\pm$ pairing in CaK(Fe$_{1-x}$Ni$_x$)$_4$As$_4$ ($x=$ 0 and 0.05) from the response to electron irradiation, Phys. Rev. B **97**, 140508(R) (2018).

[67] J.-X. Yin, X.-X. Wu, J. Li, Z. Wu, J.-H. Wang, C.-S. Ting, P.-H. Hor, X. J. Liang, C. L. Zhang, P. C. Dai, X. C. Wang, C. Q. Jin, G. F. Chen, J. P. Hu, Z.-Q. Wang, A. Li, H. Ding, and S. H. Pan, Orbital selectivity of layer-resolved tunneling in the iron-based superconductor Ba$_{0.6}$K$_{0.4}$Fe$_2$As$_2$, Phys. Rev. B **102**, 054515 (2020).

[68] K. Machida, Spin density wave and superconductivity in highly anisotropic materials, J. Phys. Soc. Jpn. **50**, 2195 (1981).

[69] R. M. Fernandes, S. A. Kivelson, and E. Berg, Vestigial chiral and charge orders from bidirectional spin-density waves: Application to the iron-based superconductors, Phys. Rev. B **93**, 014511 (2016).

[70] S. Chakravarty, Theory of the *d*-density wave from a vertex model and its implications, Phys. Rev. B **66**, 224505 (2002).

[71] H. J. Schulz, Fermi-surface instabilities of a generalized two-dimensional Hubbard model, Phys. Rev. B **39**, 2940 (1989).

[72] S. Chakravarty, R. B. Laughlin, D. K. Morr, and C. Nayak, Hidden order in the cuprates, Phys. Rev. B **63**, 094503 (2001).